Microscopic analysis of low-energy spin and orbital magnetic dipole excitations in deformed nuclei

V. O. Nesterenko [1,2,3,*] P. I. Vishnevskiy [1,2,4] J. Kvasil [5] A. Repko [6] and W. Kleinig [1]

[1]*Laboratory of Theoretical Physics, Joint Institute for Nuclear Research, Dubna, Moscow Region 141980, Russia*

[2]*State University "Dubna," Dubna, Moscow Region 141980, Russia*

[3]*Moscow Institute of Physics and Technology, Dolgoprudny, Moscow Region 141701, Russia*

[4]*Institute of Nuclear Physics, Almaty, 050032, Kazakhstan*

[5]*Institute of Particle and Nuclear Physics, Charles University, CZ-18000, Praha 8, Czech Republic*

[6]*Institute of Physics, Slovak Academy of Sciences, 84511 Bratislava, Slovakia*

(Received 26 February 2021; revised 2 May 2021; accepted 1 June 2021; published 14 June 2021; corrected 22 June 2021)

A low-energy magnetic dipole ($M1$) spin-scissors resonance (SSR) located just below the ordinary orbital scissors resonance (OSR) was recently predicted in deformed nuclei within the Wigner function moments (WFM) approach. We analyze this prediction using fully self-consistent Skyrme quasiparticle random phase approximation (QRPA) method. Skyrme forces SkM*, SVbas, and SG2 are implemented to explore SSR and OSR in ^{160,162,164}Dy and ^{232}Th. Accuracy of the method is justified by a good description of $M1$ spin-flip giant resonance. The calculations show that isotopes ^{160,162,164}Dy indeed have at 1.5–2.4 MeV (below OSR) $I^\pi K = 1^+1$ states with a large $M1$ spin strength (K is the projection of the total nuclear moment to the symmetry z axis). These states are almost fully exhausted by $pp[411\uparrow, 411\downarrow]$ and $nn[521\uparrow, 521\downarrow]$ spin-flip configurations corresponding to $pp[2d_{3/2}, 2d_{5/2}]$ and $nn[2f_{5/2}, 2f_{7/2}]$ structures in the spherical limit. So the predicted SSR is actually reduced to low-orbital ($l = 2, 3$) spin-flip states. Following our analysis and in contradiction with WFM spin-scissors picture, deformation is not the principle origin of the low-energy spin $M1$ states but only a factor affecting their features. The spin and orbital strengths are generally mixed and exhibit interference: weakly destructive in SSR range and strongly constructive in OSR range. In ^{232}Th, the $M1$ spin strength is very small. Two groups of $I^\pi = 1^+$ states observed experimentally at 2.4–4 MeV in ^{160,162,164}Dy and at 2–4 MeV in ^{232}Th are mainly explained by fragmentation of the orbital strength. Distributions of nuclear currents in QRPA states partly correspond to the isovector orbital-scissors flow but not to the spin-scissors one.

DOI: 10.1103/PhysRevC.103.064313

I. INTRODUCTION

Magnetic dipole excitations in nuclei provide important information on the nuclear spin and orbital magnetism [1,2]. For a long time, these excitations were mainly represented by $M1(K = 1)$ spin-flip giant resonance located at the energy $E \approx 41A^{-1/3}$ MeV [1,2] and low-energy $M1$ OSR with excitation energy $E \approx 66\delta A^{-1/3}$ MeV [2], where δ is the parameter of nuclear axial quadrupole deformation. Both resonances are isovector and characterized by enhanced $M1(\Delta K)$ transitions to the ground state.

The spin-flip resonance is produced by particle-hole spin-flip transitions between spin-orbit partners in the proton and neutron single-particle spectra. This resonance is related to *spin* nuclear magnetic properties and it exists in both spherical and deformed nuclei [1,2]. The spin-flip resonance was widely applied to test a spin channel in various self-consistent approaches (Skyrme, Gogny, and relativistic) [2–8] and to check tensor forces [3,4,9] and spin-orbit interaction [3–5,8].

OSR is macroscopically treated as scissors-like out-of-phase oscillations of proton and neutron deformed subsystems; see Fig. 1(a). This isovector resonance can exist only in deformed nuclei. It represents a remarkable example of a nuclear *orbital* magnetism. OSR was predicted in the two-rotor model [10,11] and then experimentally observed in (e, e') reaction [12]. OSR demonstrates some specific features: linear and square deformation laws for its energy and strength, respectively [13,14]. Various properties of OSR are outlined in reviews [2,15,16]. OSR is a kind of mixed-symmetry state [17–19]. Recent studies of OSR can be found elsewhere; see, e.g., Refs. [20–22].

A decade ago, Balbutsev, Molodtsova, and Schuck have predicted [within the Wigner function moments (WFM) method] that OSR should be supplemented by a low-energy *spin*-scissor mode (SSR) [23]. Further WFM calculations with inclusion of the pairing [24–26] and isoscalar-isovector coupling in the residual interaction [27–29] have shown that SSR should have two branches [see Figs. 1(b) and 1(c)] lying below OSR. Thus, altogether the nuclear scissors mode should be a triplet: OSR + two SSR branches. All the scissors states should demonstrate significant $M1(\Delta K = 1)$ transitions to the ground state.

Following the WFM calculations, SSR should exist in medium and heavy axial deformed nuclei, typically at the excitation energy $E < 2.7$ MeV, i.e., just below OSR [25–29]. Many $I^\pi = 1^+$ states at $E < 2.7$ MeV were already observed in rare-earth and actinide nuclei; see, e.g., Refs. [30–34].

*nester@theor.jinr.ru

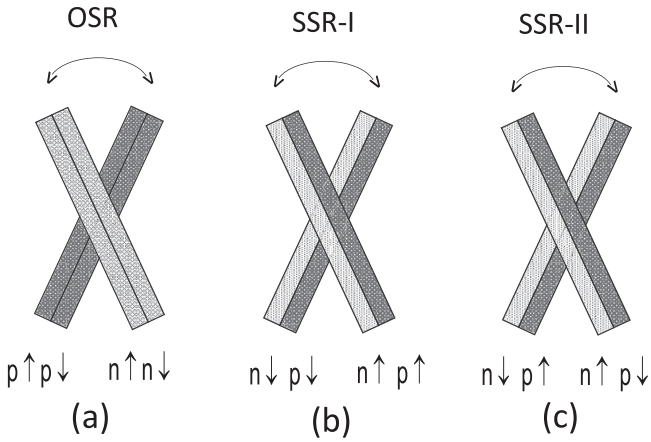

FIG. 1. The schemes for the members of the scissors triple [28]: OSR (a), SSR-I (b), and SSR-II (c). The neutron (proton) axially deformed fractions are shown by light (dark) bars. The spin direction of nucleons is indicated by arrows. Each mode in the triple exhibits scissors-like oscillations of two blades: neutrons vs protons in OSR, spin-up vs spin-down nucleons in SSR-I (spins of neutrons and protons in each blade have the same direction), and SSR-II where neutron and proton spins in each blade have opposite directions.

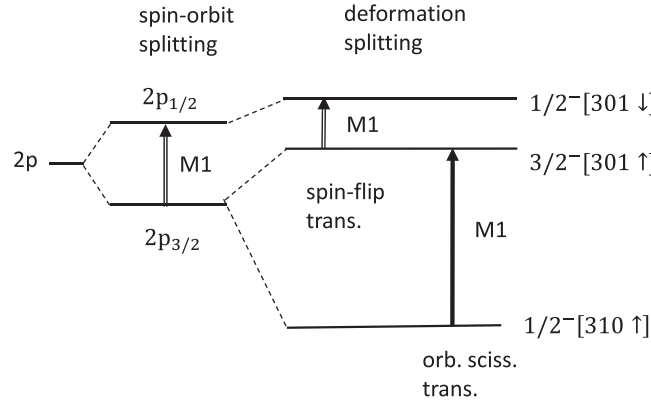

FIG. 2. A scheme of single-particle levels for $2p$ subshell in spherical (left) and deformed (right) cases. The scheme corresponds to the proton $2p$ subshell in ^{162}Dy, calculated with the Skyrme force SG2. Spin-flip and orbital scissors $M1$ transitions are exhibited by empty and filled arrows, respectively. In the deformed case, the levels are denoted by Nilsson asymptotic quantum numbers [37,38], and the arrows indicate spin direction.

However, they are usually not included in the experimental OSR systematics and their origin is still rather unclear. The prediction of SSR suggests an explanation for these states. Following the detailed WFM analysis for ^{160,162,164}Dy, ^{232}Th, and ^{236,238}U [26–29], the nuclei ^{164}Dy and ^{232}Th are the most promising candidates for SSR. Low-energy 1^+ states in these nuclei form two distinctive groups which might be attributed to SSR and OSR.

The aim of the present paper is to scrutinize the WFM prediction of SSR from the microscopic viewpoint. It is well known that both orbital and spin-flip $M1$ transitions can be explained using single-particle schemes [1,35]. An example of such a scheme for the $2p$ subshell is shown in Fig. 2. This is a fraction of the proton scheme in ^{162}Dy, calculated with Skyrme parametrization SG2 [36]. The computed equilibrium axial quadrupole deformation is $\beta_2 = 0.346$. The left part of the figure shows the splitting of the $2p$ subshell into $2p_{1/2}$ and $2p_{3/2}$ levels due to spin-orbit interaction. Already in this spherical case, a spin-flip $M1$ transition between the levels is possible. The large deformation significantly splits the level $2p_{3/2}$ and upshifts the level $2p_{1/2}$ (right part of Fig. 2). In this case, two $M1(\Delta K = 1)$ transitions are possible: spin-flip $3/2^-[301\uparrow] \to 1/2^-[301\downarrow]$ and orbital $1/2^-[310\uparrow] \to 3/2^-[301\uparrow]$. The former connects the spin-orbit partners, the latter relates the levels arising due to deformation splitting. So we get two natural candidates for SSR and OSR. Because of the large deformation splitting, the orbital transition has a larger energy than the spin-flip one. So SSR should lie lower by energy than OSR.

As seen in Figs. 1(b) and 1(c), neutrons and protons in the left and right scissors blades have opposite spin directions. Perhaps the predicted SSR can be somehow related to spin-flip excitations in neutron and proton spectra. This point is yet unclear (see discussion in Appendix B). It is important that Fig. 2 clearly shows that nuclear deformation is not the primary origin of low-energy spin-flip states (though it can significantly affect their features). This means that WFM interpretation of low-energy spin states in terms of *deformation-induced scissors* oscillations is questionable.

The main aim of the present study is to show that the predicted low-energy spin states are ordinary spin-flip excitations and the available experimental data can be explained by the fragmentation of spin-flip and orbital $M1$ strength. Our analysis is performed for axially deformed nuclei ^{160,162,164}Dy and ^{232}Th. As mentioned above, two of these nuclei, ^{164}Dy and ^{232}Th, are considered by WFM as promising candidates for SSR. The calculations are performed using fully self-consistent QRPA [39–44] with the Skyrme forces SG2 [36], SkM* [45], and SVbas [46]. As shown below, the spin and orbital low-energy $M1$ excitations are strongly mixed. So we will analyze both SSR and OSR. To demonstrate accuracy of our calculations, we will also present results for $M1$ spin-flip giant resonance.

The paper is organized as follows. In Sec. II, the calculation scheme is outlined. In Sec. III, results of the calculations are discussed. In particular, flows of the nuclear currents are exhibited. In Sec. IV, the conclusions are drawn. In Appendix A, a description of the $M1$ spin-flip giant resonance is illustrated. In Appendix B, some important aspects of WFM/QRPA comparison are discussed. In Appendix C, expressions for the orbit and spin transition matrix elements are given.

II. CALCULATION SCHEME

The calculations are performed within the Skyrme QRPA model [39–44]. The model is fully self-consistent, i.e., (i) both mean field and residual interaction are derived from the initial Skyrme functional, (ii) the residual interaction takes into account all the terms of the Skyrme functional and Coulomb (direct and exchange) parts, and (iii) both particle-hole and particle-particle channels are included [42].

TABLE I. Isoscalar effective mass m_0^*, isoscalar and isovector spin-orbit parameters b_4 and b'_4, proton and neutron pairing constants G_p and G_n, and the type of pairing in Skyrme forces SkM*, SVbas, and SG2.

Force	m_0^*	b_4 (MeV fm^5)	b'_4 (MeV fm^5)	G_p (MeV fm^3)	G_n (MeV fm^3)	Pairing
SkM*	0.79	65.0	65.0	279.08	258.96	Volume
SVbas	0.90	62.32	34.11	674.62	606.90	Surface
SG2	0.79	52.5	52.5	296.76	259.58	Volume

Spurious admixtures caused by violation of the rotational invariance are removed using the SEBRPA (spuriosity extracted before RPA) technique[44].

A representative set of Skyrme forces is used. We employ the standard force SkM* [45], the recently developed force SVbas [46], and the force SG2 [36], which is often used in analysis of magnetic excitations; see, e.g., Refs. [4,5,47]. As seen from Table I, these forces have different isoscalar b_4 and isovector b'_4 parameters of the spin-orbit terms in the Skyrme functionals (see definitions of the parameters in Refs. [4,40]). In SkM* and SG2, the usual convention $b_4 = b'_4$ is used while in SVbas a separate tuning of b_4 and b'_4 is done. All three Skyrme forces reproduce, though with different degrees of accuracy, a two-hump structure of $M1$ spin-flip giant resonance in deformed nuclei [4,5]. As shown in Appendix A, SVbas and especially SG2 give a nice description of this resonance. So these two Skyrme forces can be considered as the most relevant for the present study.

The nuclear mean field and pairing are computed with the code SKYAX [48] using a two-dimensional grid in cylindrical coordinates. The calculation box extends up to three times the nuclear radii, and the grid step is 0.4 fm. The axial quadrupole equilibrium deformation is obtained by minimization of the energy of the system. As seen from Table II, the obtained values of the deformation parameter β are in a good agreement with the experimental data [49], especially for SVbas. All the forces reproduce a growth of the deformation from ^{160}Dy to ^{164}Dy.

Pairing is described by the zero-range pairing interaction [51]

$$V^q_{\rm pair}(\mathbf{r},\mathbf{r}') = G_q\Big[1-\eta\left(\frac{\rho(\mathbf{r})}{\rho_{\rm pair}}\right)\Big]\delta(\mathbf{r}-\mathbf{r}'), \qquad (1)$$

TABLE II. Calculated parameters β of the equilibrium axial quadrupole deformation vs the experimental values [49].

Nucleus	β SkM*	SVbas	SG2	Exper.
^{160}Dy	0.339	0.331	0.339	0.334 (2)
^{162}Dy	0.351	0.345	0.346	0.341(3)
^{164}Dy	0.354	0.348	0.352	0.349(3)
^{232}Th	0.256	0.247	0.238	0.248 (6)

TABLE III. Proton and neutron pairing gaps Δ_p and Δ_n and energy of 2^+_1 state of the ground-state rotational band, calculated in ^{162}Dy and ^{232}Th with Skyrme forces SkM*, SVbas, and SG2. The experimental data for the energy $E_{2^+_1}$ are taken from database [49].

Nucleus		SkM*	SVbas	SG2	exper.
^{162}Dy	Δ_p [MeV]	0.55	0.69	0.72	
	Δ_n [MeV]	0.62	0.95	0.87	
	$E_{2^+_1}$ [keV]	67.9	92.7	88.8	80.7
^{232}Th	Δ_p [MeV]	0.53	0.61	0.75	
	Δ_n [MeV]	0.54	0.80	0.78	
	$E_{2^+_1}$ [keV]	41.2	57.1	63.0	49.4

where G_q are proton ($q = p$) and neutron ($q = n$) pairing strength constants. They are fitted to reproduce empirical pairing gaps obtained by the five-point formula along selected isotopic and isotonic chains [50]. The values of G_q are shown in Table I. Further, $\rho(\mathbf{r}) = \rho_p(\mathbf{r}) + \rho_n(\mathbf{r})$ is the sum of proton and neutron densities. We get so-called volume pairing for $\eta = 0$ and density-dependent surface pairing for $\eta = 1$. As indicated in Table I, the former is used in SkM* and SG2, and the latter is exploited in SVbas. In the latter case, we use SVbas parameter $\rho_{\rm pair} = 0.2011\,{\rm fm}^{-3}$. Pairing correlations are included at the level of the iterative HF-BCS (Hartree-Fock plus Bardeen-Cooper-Schrieffer) method [42]. To cope with the divergent character of zero-range pairing forces, energy-dependent cutoff factors are used [42,51].

Table III shows the calculated averaged proton and neutron pairing gaps Δ_p and Δ_n (defined in Eq. (30) of Ref. [51]) in ^{162}Dy and ^{232}Th. Also we exhibit the energies $E_{2^+_1} = 3\hbar^2/\mathcal{J}$ (with $\mathcal{J}$ being the nuclear moment of inertia) of $I^\pi = 2^+$ state in the ground-state rotational band. These energies are sensitive to both deformation and pairing. As seen from Table III, SkM* underestimates while SVbas and SG2 somewhat overestimate the experimental $E_{2^+_1}$ values.

In our calculations, QRPA is implemented in the matrix form. A large configuration space is used. The single-particle spectrum extends from the bottom of the potential well up to 30 MeV. For example, in SG2 calculations for ^{162}Dy, 691 proton and 800 neutron single-particle levels are used. The two-quasiparticle (2qp) basis in QRPA calculation for $K^\pi = 1^+$ states includes 5270 proton and 9527 neutron configurations. We do not consider $K^\pi = 0^+$ excitations since it is well known [1,2,15,16] that $M1$ spin-flip and orbital-scissors modes are characterized by strong $M1(\Delta K = 1)$ transitions to the ground state.

Reduced probability for $M1$ transitions from the ground state $|0\rangle$ with $I^\pi K = 0^+0$ to the excited QRPA state $|\nu\rangle$ with $I^\pi K = 1^+1$ reads

$$B_\nu(M1) = 2|\,\langle\nu|\,\hat\Gamma(M11)\,|0\rangle\,|^2. \qquad (2)$$

The coefficient 2 means that contributions of both projections $K = 1$ and -1 are taken into account. The transition operator has the form

$$\hat\Gamma(M11) = \mu_N\sqrt{\frac{3}{4\pi}}\sum_{q=p,n}[g^q_s\hat s(\mu=1) + g^q_l\hat l(\mu=1)], \qquad (3)$$

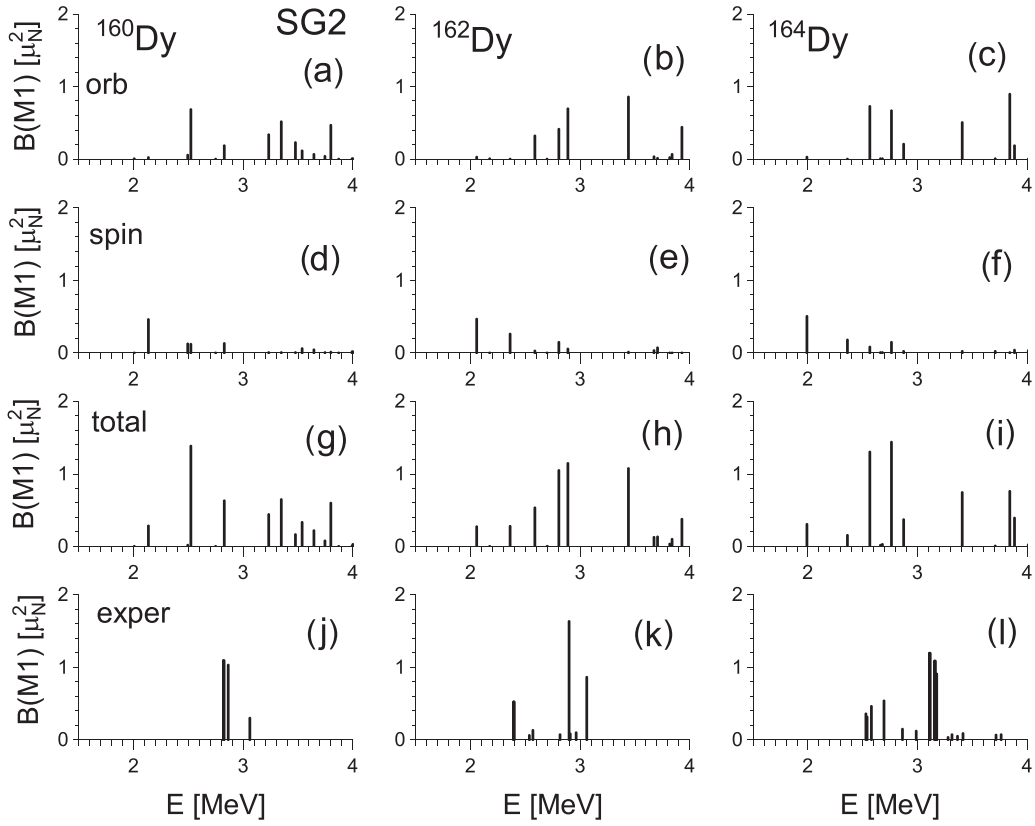

FIG. 3. Orbital [(a)–(c)], spin [(d)–(f)], and total [(g)–(i)] low-energy $M1$ strength in ^{160,162,164}Dy, calculated in QRPA with Skyrme force SG2. In the bottom panels, the experimental $M1$ strength for ^{160}Dy [30] and ^{162,164}Dy [31] is shown.

where μ_N is the nuclear magneton, $\hat{s}(\mu = 1)$ and $\hat{l}(\mu = 1)$ are $\mu = 1$ projections of the standard spin and orbital operators, and g_s^q and g_l^q are spin and orbital gyromagnetic factors. We use the quenched spin g factors $g_s^q = \eta \bar{g}_s^q$, where $\bar{g}_s^p = 5.58$ and $\bar{g}_s^n = -3.82$ are bare proton and neutron g factors and $\eta = 0.7$ is the quenching parameter [1]. The orbital g factors are $g_l^p = 1$ and $g_l^n = 0$. In what follows, we consider three cases: spin ($g_l^q = 0$), orbital ($g_s^q = 0$), and total (when both spin and orbital transitions are taken into account). The expressions for orbital and spin $M1$ matrix elements are given in Appendix C.

In deformed nuclei, electric and magnetic states with the same K^π are mixed [1,15,35,52]. In our case of $K^\pi = 1^+$ states, the magnetic dipole $M1(K = 1)$ and electric quadrupole $E2(K = 1)$ modes can be mixed. To estimate this mixing, we calculate reduced probability of $E2$ transitions $0^+0 \to 2^+1$:

$$B_\nu(E2) = 2|\,\langle\nu|\,\hat{\Gamma}(E21)\,|0\rangle\,|^2 \tag{4}$$

with the proton transition operator

$$\hat{\Gamma}(E21) = er^2 Y_{21}(\theta, \phi), \tag{5}$$

where $Y_{21}(\theta, \phi)$ is the spherical harmonic.

We also calculate the current transition densities (CTD)

$$\delta\mathbf{j}_\nu(\mathbf{r}) = \langle\nu|\hat{\mathbf{j}}|0\rangle(\mathbf{r}) \tag{6}$$

for the convective nuclear current

$$\hat{\mathbf{j}}(\mathbf{r}) = -i\frac{e\hbar}{2m}\sum_{q=n,p} e_{\rm eff}^q \sum_{k\epsilon q}[\delta(\mathbf{r}-\mathbf{r}_k)\nabla_k + \nabla_k\delta(\mathbf{r}-\mathbf{r}_k)]. \tag{7}$$

Here $e_{\rm eff}^q$ are the effective charges. They are $e_{\rm eff}^p = 1$ and $e_{\rm eff}^n = 0$ for the proton current, $e_{\rm eff}^p = 0$ and $e_{\rm eff}^n = 1$ for the neutron current, and $e_{\rm eff}^p = e_{\rm eff}^n = 1$ for the isoscalar current and $e_{\rm eff}^p = -e_{\rm eff}^n = 1$ for the isovector current.

Beside, we calculate the separate spin-up and spin-down parts of CTD (6). For this aim, the wave function of the QRPA state $|\nu\rangle$ is projected to the proper spin direction using spinor structure of the involved single-particle wave functions in cylindric coordinates; see Eqs. (C1) and (C2) in Appendix C.

III. RESULTS AND DISCUSSION

A. $M1$ strength in ^{160,162,164}Dy

In Fig. 3, we compare calculated orbital, spin, and total $M1$ strengths (2) in ^{160,162,164}Dy with experimental data from the nuclear resonance fluorescence (NRF) reaction; see Refs. [30] for ^{160}Dy and [31] for ^{162,164}Dy. QRPA results are obtained for the force SG2. Following the discussion in Sec. II and results for the spin-flip $M1$ giant resonance in Appendix A, this force seems to be the most relevant for our analysis.

Figures 3(a)–3(c) show that $M1$ strength above 2.4 MeV is mainly orbital. This strength constitutes the OSR. Instead, a

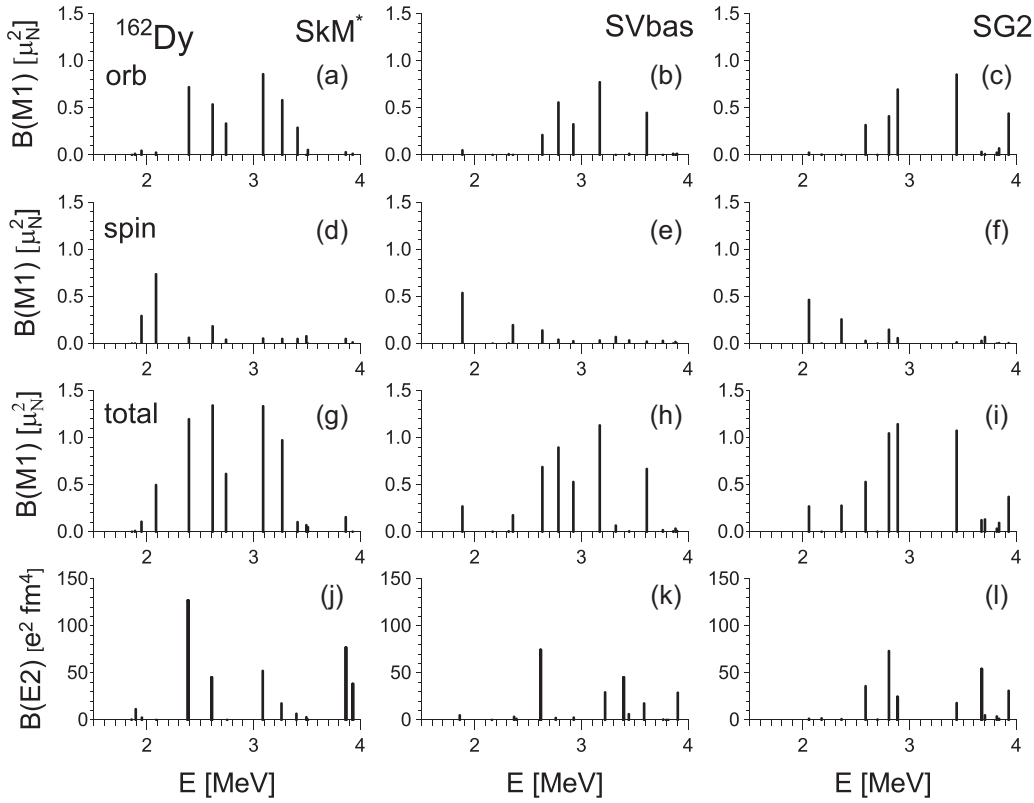

FIG. 4. Orbital [(a)–(c)], spin [(d)–(f)], and total [(g)–(i)] low-energy $M1$ strength in ^{162}Dy, calculated in QRPA with Skyrme forces SkM* (left), SVbas (middle), and SG2 (right). In the bottom panels, the quadrupole $E2$ strength is shown.

few states at $E < 2.4$ MeV exhibit a noticeable spin strength; see Figs. 3(d)–3(f). Following prediction [25–29], these states are candidates for SSR. Comparing spin and orbital strengths with the total one [Figs. 3(g)–3(i)], we see that spin and orbital modes have a strong interference, both destructive and constructive. These results take place for all three Dy isotopes.

Figure 3 shows that NRF data [30,31] do not give $I^\pi = 1^+$ states at $E < 2.39$ MeV. As discussed in Ref. [33], this may be caused by troubles of traditional NRF experiments to separate transitions in this energy range from a sizable background. The early data for ^{160}Dy [30] give 1^+ states only for $E > 2.8$ MeV, though the level list in database [49] suggests many candidates for 1^+ states at lower excitation energies.

In ^{162,164}Dy, NRF data [31] give two groups of 1^+ states located above and below 2.7 MeV. The former group is usually treated as OSR. The latter is treated by WFM as SSR [25–29]. Note that low-energy groups of 1^+ states were earlier observed in various rare-earth nuclei [30]. Recent Oslo (γ, n) experiment [33] shows that, in ^{164}Dy, 40–60% of $M1$ strength at energy range 0–4 MeV is located below 2.7 MeV. Moreover, in this nucleus the total measured $M1$ strength at 0–4 MeV achieves 6.17 μ_N^2 [31], which substantially exceeds the values 3–4 μ_N^2 typical for OSR in well-deformed rare-earth nuclei. This observation was treated by WFM as a clear signature of SSR in ^{164}Dy [25–29]. However, following our results in Fig. 3, the states at 2.4–2.7 MeV give mainly orbital $M11$ transitions and so should also belong to OSR. They are omitted in OSR systematics with the lower boundary 2.7 MeV [52] but taken into account for the lower boundary 2.5 MeV [20]. So, by our opinion, the data of Oslo group cannot be considered as the argument in favor of SSR.

In Fig. 4, we demonstrate the distribution of $M1$ strength in ^{162}Dy, calculated with the forces SkM*, SVbas, and SG2. It is seen that, despite some deviations in details, all these three forces give qualitatively similar results. In all cases, there is the range 0–2.4 MeV with an essential spin strength and the range 2.4–4.0 MeV with a dominant orbital strength. Figure 4 also demonstrates $E2$ strength (4) for the same $K^\pi = 1^+$ states. This strength is large at 2.6–4.0 MeV and negligible at 0–2.6 MeV. The former result is typical for OSR [15,52]. This means that OSR states are mixtures of $M1(K = 1)$ and $E2(K = 1)$ modes, which is common in well-deformed nuclei.

Note that, in WFM calculations for ^{164}Dy [27–29], the lowest $K^\pi = 1^+$ state at 1.47 MeV has a huge quadrupole strength $B(E2) = 25.44$ W.u. (≈ 1300 e^2 fm^4). The authors do not explain the origin of this state. Besides, for the next state at 2.20 MeV, Figs. 9(a) and 9(b) in Ref. [28] show a spurious-like isoscalar flow. By our opinion, the 1.47-MeV state is spurious, and higher states can also have spurious admixtures despite the statements [27–29] that spurious modes are extracted in WFM by construction. Note that similar lowest-by-energy spurious states appear in QRPA calculations if the 2qp basis is insufficient and/or the procedure for removal of spurious states is not exact. Our QRPA calculations for ^{160,162,164}Dy (with accurate extraction of spurious admixtures by method in Ref. [44]) do not give low-energy $K^\pi = 1^+$ states with high $B(E2)$; see, e.g., Fig. 4. Moreover, such states are not

TABLE IV. The calculated orbital, spin, and total strengths $\sum B(M1)$ (in μ_N^2) in ^{160,162,164}Dy, summed at SSR (0–2.4 MeV), OSR (2.4–4 MeV), and total (0–4 MeV) energy ranges as compared with experimental data for ^{160}Dy [30] and ^{162,164}Dy [31]. For each energy range, the interference factors R are shown.

		0–2.4 MeV				2.4–4 MeV				0–4 MeV				
		$\sum B(M1)$				$\sum B(M1)$				$\sum B(M1)$				
Nucleus	Force	Orb	Spin	Total	R	Orb	Spin	Total	R	Orb	Spin	Total	Exp	R
	SkM*	0.52	0.96	1.32	0.89	2.79	0.55	4.85	1.45	3.31	1.51	6.16		1.28
^{160}Dy	SVbas	0.05	0.49	0.23	0.43	2.15	0.51	3.80	1.43	2.20	1.00	4.03	2.42	1.26
	SG2	0.03	0.46	0.28	0.57	2.69	0.54	4.53	1.40	2.72	1.00	4.81		1.29
	SkM*	0.80	1.09	1.80	0.95	2.69	0.51	4.63	1.45	3.49	1.60	6.44		1.27
^{162}Dy	SVbas	0.06	0.73	0.45	0.57	2.35	0.40	4.04	1.47	2.41	1.14	4.49	3.45	1.26
	SG2	0.03	0.72	0.55	0.73	2.85	0.35	4.54	1.42	2.88	1.07	5.09		1.29
	SkM*	0.96	1.09	2.11	1.03	2.18	0.40	3.94	1.53	3.14	1.49	6.05		1.31
^{164}Dy	SVbas	0.06	0.63	0.32	0.47	2.52	0.50	4.37	1.45	2.57	1.13	4.69	6.17	1.27
	SG2	0.03	0.68	0.45	0.63	3.20	0.35	5.05	1.42	3.23	1.03	5.50		1.29

known experimentally and, to our knowledge, absent in other microscopic calculations; see, e.g., Ref. [53] for ^{164}Dy.

In Table IV, we show spin, orbital, and total QRPA strengths $\sum B(M1)$ summed in the SSR (0–2.4 MeV), OSR (2.4–4 MeV), and SSR + OSR (0–4 MeV) energy intervals. The total QRPA strengths are compared with NRF experimental data for 1^+ states observed at 2.8–3.1 MeV in ^{160}Dy [30]), 2.3–3.1 MeV in ^{162}Dy [31], and 2.5–3.8 MeV in ^{164}Dy [31].

Table IV shows that at 0–2.4 MeV the spin strength dominates over the orbital one. For SkM*, the orbital fraction in this interval is also essential. In the OSR region 2.4–4 MeV, the orbital $M1$ strength strongly dominates though the spin strength is large as well.

Following Table IV, QRPA total $M1$ strengths summed at 0–4 MeV significantly overestimate the experimental values in ^{160,162}Dy but generally correspond to the experiment in ^{164}Dy (SkM* and SG2). Perhaps, as mentioned above, the experimental data for ^{160,162}Dy [30,31] miss a significant part of $M1$ strength. Also, the present calculations do not take into account a coupling with complex configurations which can spread the strength and so decrease $\sum B(M1)$ values at 0–4 MeV. Our results significantly depend on the applied Skyrme force. For example, in all considered nuclei, SVbas gives much smaller orbital and total strengths than SkM* and SG2. This can be explained by a stronger pairing in SVbas (see discussion of Table III in Sec. II), which upshifts a part of $M1$ strength above 4 MeV.

In both SSR and OSR regions, we see an interference between spin and orbital contributions to the total strength (i.e., the sum of spin and orbital contributions does not equal to the total strength). It is convenient to estimate this effect by an interference factor

$$R = \frac{\sum B(M1)_t}{\sum B(M1)_o + \sum B(M1)_s}, \tag{8}$$

where $\sum B(M1)_o$, $\sum B(M1)_s$, and $\sum B(M1)_t$ are summed orbital, spin, and total strengths. The interference is destructive at $R < 1$, constructive at $R > 1$, and absent at $R = 1$.

Table IV shows that the interference is destructive in SSR range (with exception of SkM* case in ^{164}Dy) and constructive in OSR range. *The interference greatly increases the role of the minor spin fraction in the OSR range.* For example, in ^{162}Dy (SG2), the interference results in the total strength $4.54\,\mu_N^2$, which is much larger than the orbital strength $2.85\,\mu_N^2$.

Our results generally agree with the study of low-energy (0–4 MeV) $K^\pi = 1^+$ states in ^{160,162,164}Dy, performed within the quasiparticle-phonon nuclear model (QPNM) [53]. This model is not self-consistent. However, it has an advantage of taking into account the coupling with complex configurations. In agreement with our results, QPNM also predicts in Dy isotopes a well-separated group of 1^+ states located at 2–2.6 MeV and carrying a noticeable fraction of spin $M1$ strength. However, in QPNM the total strength of these states is mainly orbital. Only in two states at 2.0–2.1 MeV in ^{164}Dy does spin contribution to $M1$ strength dominate over the orbital one. Coupling with complex configurations is found strong in OSR region and weaker for lower excitations. This effect can additionally downshift the orbital strength to the lower SSR region. QPNM also predicts a considerable interference between spin and orbital contributions.

For a better understanding of our results, it is worth considering the structure and other features of the most interesting 1^+ states. They are shown for ^{162}Dy in Table V. We present two states with the largest spin strength $B(M1)_s$ and one state with the largest orbital strength $B(M1)_o$. In the spin states, we have $B(M1)_s > B(M1)_o$. Their main 2qp components, proton $[411\uparrow, 411\downarrow]$ and neutron $[521\uparrow, 521\downarrow]$, are of the spin-flip character and correspond to particle-hole (1ph) transitions. Note that the same spin-flip 2qp configurations were found in QPNM calculations [53] for low-energy 1^+ states in Dy isotopes. In the spherical limit, these configurations are reduced to spin-flip partners $2d_{5/2}, 2d_{3/2}$ and $2f_{7/2}, 2f_{5/2}$ with low orbital moments $l = 2$ and 3. For low l, the spin-orbit energy splitting $\sim(\mathbf{l}\cdot\mathbf{s})$ is small and leads to low-energy spin-flip excitations. The states with larger l contribute to the spin-flip giant resonance located at a higher energy. Altogether, we see that *so-called SSR states are actually ordinary low-energy noncollective spin-flip excitations*.

TABLE V. Characteristics of some relevant low-energy $K^{\pi}_{\nu} = 1^{+}_{\nu}$ states in ^{162}Dy, calculated within QRPA with the forces SkM*, SVbas, and SG2. For each state, we show the excitation energy E, orbital, spin, and total reduced transition probabilities $B(M1)$ and main 2qp components (contribution to the state norm in %, structure in terms of Nilsson asymptotic quantum numbers, position of the involved single-particle states relative to the Fermi level F, and original quantum subshells in the spherical limit).

Force	ν	E	$B(M1)$ [μ_N^2]			Main 2qp components			
		[MeV]	Orb	Spin	Total	%	$[N, n_z, \Lambda]$	F position	Spher. limit
SkM*	3	1.95	0.05	0.29	0.11	69	pp [411 ↑, 411 ↓]	$F-1, F+1$	$2d_{5/2}, 2d_{3/2}$
						30	nn [521 ↑, 521 ↓]	$F-1, F+2$	$2f_{7/2}, 2f_{5/2}$
	4	2.08	0.02	0.73	0.50	69	nn [521 ↑, 521 ↓]	$F-1, F+2$	$2f_{7/2}, 2f_{5/2}$
						28	pp [411 ↑, 411 ↓]	$F-1, F+1$	$2d_{5/2}, 2d_{3/2}$
	8	3.09	0.86	0.05	1.33	61	nn [521 ↑, 512 ↑]	$F-1, F+4$	$2f_{7/2}, 2f_{7/2}$
						25	pp [411 ↑, 402 ↑]	$F-1, F+4$	$2d_{5/2}, 2d_{5/2}$
SVbas	1	1.88	0.05	0.54	0.27	97	pp [411 ↑, 411 ↓]	$F, F+1$	$2d_{5/2}, 2d_{3/2}$
						2	nn [521 ↑, 521 ↓]	$F-1, F+2$	$2f_{7/2}, 2f_{5/2}$
	4	2.36	≈ 0	0.20	0.18	94	nn [521 ↑, 521 ↓]	$F-1, F+2$	$2f_{7/2}, 2f_{5/2}$
						2	pp [411 ↑, 411 ↓]	$F, F+1$	$2d_{5/2}, 2d_{3/2}$
	8	3.17	0.77	0.04	1.13	65	nn [521 ↑, 512 ↑]	$F-1, F+4$	$2f_{7/2}, 1h_{9/2}$
						16	pp [413 ↓, 404 ↓]	$F-2, F+4$	$1g_{7/2}, 1g_{7/2}$
SG2	1	2.06	0.03	0.46	0.27	99	pp [411 ↑, 411 ↓]	$F, F+1$	$2d_{5/2}, 2d_{3/2}$
	3	2.36	≈ 0	0.26	0.28	99	nn [521 ↑, 521 ↓]	$F-1, F+2$	$2f_{7/2}, 2f_{5/2}$
	8	3.44	0.86	0.01	1.07	57	nn [521 ↑, 512 ↑]	$F-1, F+4$	$2f_{7/2}, 1h_{9/2}$
						31	pp [413 ↓, 404 ↓]	$F-2, F+4$	$1g_{7/2}, 1g_{7/2}$

The orbital and spin-flip $M1$ transitions in ^{162}Dy can be illustrated using neutron and proton single-particle level schemes. In Fig. 5, we show a proton scheme for $2d$ subshell, calculated with SG2 at the equilibrium deformation $\beta = 0.346$. This scheme demonstrates the same physical mechanisms as in Fig. 2 but now for the case including the proton spin-flip transition $3/2^+[411\uparrow] \to 1/2^+[411\downarrow]$ which is of our interest. We see that the low-energy spin-flip transition $2d_{5/2} \to 2d_{3/2}$ can take place already in the spherical case. In the deformed case, two spin-flip and three orbital $M1$ transitions are possible. However, only two of these transitions are of 1ph character and so not suppressed (other transitions can appear only due to the pairing). They are spin-flip $3/2^+[411\uparrow] \to 1/2^+[411\downarrow]$ and orbital $3/2^+[411\uparrow] \to 5/2^+[402\uparrow]$. As seen from Table V, the proton spin-flip 2qp configuration $[411\uparrow, 411\downarrow]$ indeed dominates in the states at 1.95 (SkM*), 1.88 (SVbas), and 2.06 MeV (SG2). The orbital configuration $[411\uparrow, 402\uparrow]$ is fragmented between many states; it is seen, e.g., in 3.09-MeV state (SkM*). Since deformations in ^{160,162,164}Dy are similar (see Table II), the same results should take place for ^{160}Dy and ^{164}Dy as well.

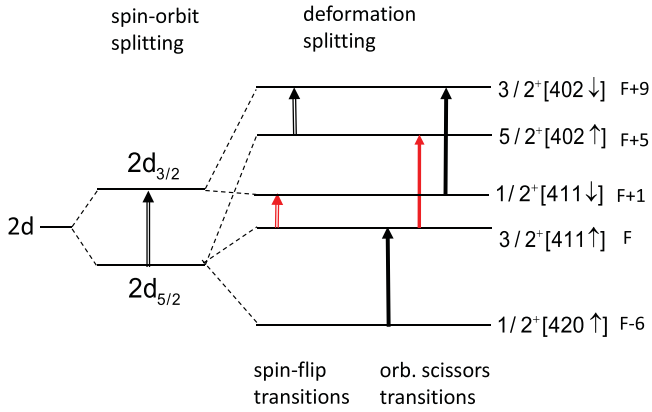

FIG. 5. A calculated (SG2) scheme of spin-flip (left empty arrows) and orbital scissors (right filled arrows) $M1$ transitions in the proton $2d$ subshell in ^{162}Dy. As indicated in the top inscriptions, the left part of the figure demonstrates a spin-orbit splitting into $2d_{3/2}$ and $2d_{5/2}$ levels in the spherical case, while the right part exhibits an additional deformation splitting. In the deformed case, $M1(\Delta K) = 1$ transitions form two groups, spin-flip and orbital scissors, as indicated in the bottom inscriptions. The Fermi level is $3/2^+[411\uparrow]$. The 1ph transitions, spin-flip $3/2^+[411\uparrow] \to 1/2^+[411\downarrow]$ and orbital $3/2^+[411\uparrow] \to 5/2^+[402\uparrow]$, are marked by red color.

A similar analysis can be done for a neutron single-particle scheme in ^{162}Dy. A relevant part of this scheme for $2f$ subshell is shown in Fig. 6. We see that again, among many possible spin-flip and orbital $M1$ transitions, there are only two 1ph transitions: spin-flip $3/2^-[521\uparrow] \to 1/2^-[521\downarrow]$ and orbital $3/2^-[521\uparrow] \to 5/2^-[512\uparrow]$. The corresponding 2qp configurations indeed take place in Table V.

It is easy to recognize from Fig. 6 that ^{160}Dy and ^{164}Dy, whose Fermi levels correspond to $F-1$ and $F+1$ states of the given neutron scheme, also allow 1ph spin-flip transitions $3/2^-[521\uparrow] \to 1/2^-[521\downarrow]$. This explains why in our calculations all three isotopes ^{160,162,164}Dy demonstrate similar distributions of low-lying spin-flip excitations.

B. Nuclear currents in ^{162}Dy

In this section, we show various CTD $\delta\mathbf{j}_{\nu}(\mathbf{r})$ defined in Sec. II. CTD are calculated with the force SG2 for a few relevant states in ^{162}Dy, shown in Table V. First, we consider 3.44-MeV state which, following Fig. 4, demonstrates the largest orbital $M1$ strength. Figure 7 shows for this state the proton, neutron, isoscalar ($\Delta T = 0$), and isovector ($\Delta T = 1$)

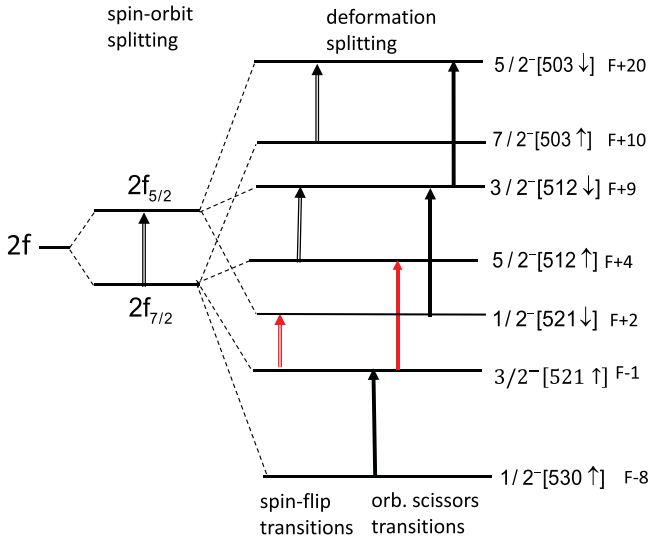

FIG. 6. The same as in Fig. 5 but for the neutron $2f$ subshell in ^{162}Dy. The $1ph$ spin-flip $3/2^-[521\uparrow] \rightarrow 1/2^-[521\downarrow]$ and orbital $3/2^-[521\uparrow] \rightarrow 5/2^-[512\uparrow]$ transitions are marked by red color.

CTD plotted on (x, z) plane, where z is the nuclear symmetry axis. Magnitudes of the currents are equally scaled to provide distinctive pictures. So, only relative lengths of the current arrows and their directions (but not absolute lengths of arrows) are matter. The nuclear boundary estimated for the sharp nucleus edge is depicted by a solid ellipse.

Figure 7 shows that protons and neutrons in the 3.44-MeV state move in opposite directions at the left and right

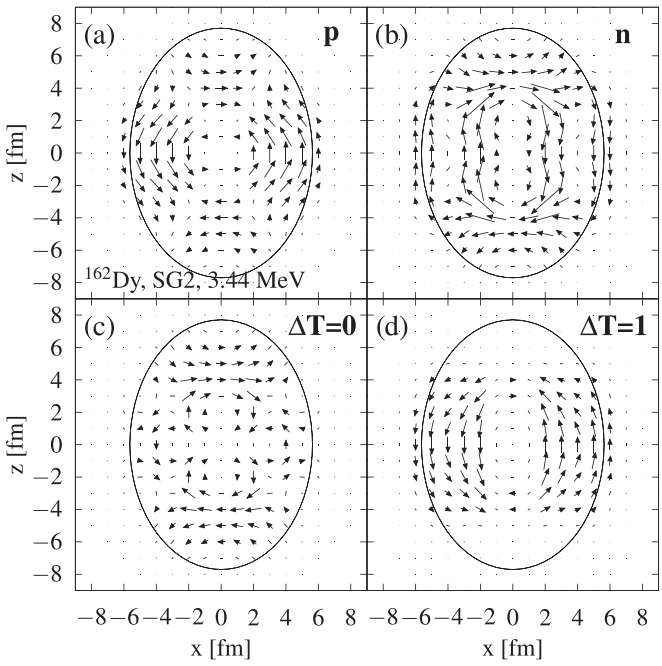

FIG. 7. Proton (a), neutron (b), isoscalar (c), and isovector (d) convection CTD in (x, z) plane for 3.44-MeV state in ^{162}Dy, calculated within QRPA with the force SG2. A solid ellipse shows the nuclear boundary.

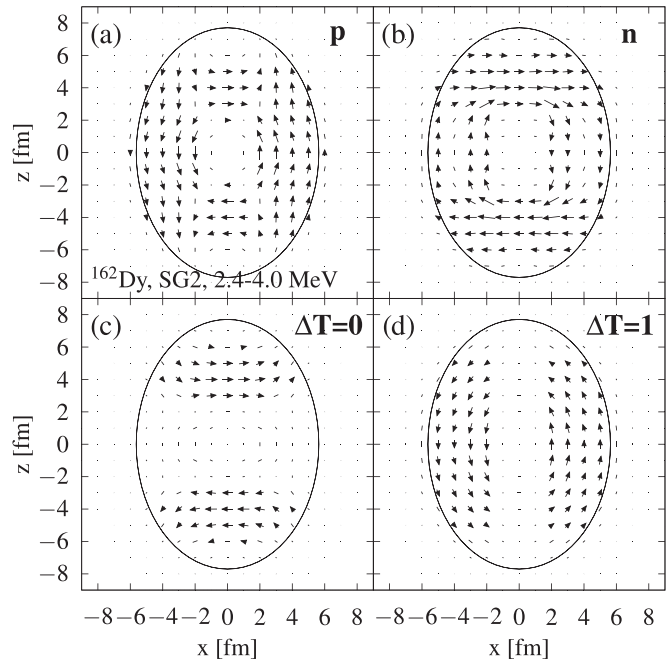

FIG. 8. The same as in Fig. 7 but for the energy interval 2.4–4 MeV.

surface regions [cf. Figs. 7(a), 7(b) and 7(d)] and this motion resembles an isovector OSR (a similar orbital current was earlier obtained in deformed ^{50}Cr [21]). Following Table V, the 3.44-MeV state has large proton (57%) and neutron (31%) 2qp components. This complicates a general flow and makes it different (in the pole regions) from the simple collective OSR picture. We also see that 3.44-MeV state exhibits both isoscalar and isovector currents.

For a reasonable comparison with collective WFM currents, it is worth considering the *summed* CTD involving contributions of all QRPA states from the OSR energy range 2.4–4 MeV. The summed CTD will smooth individual peculiarities of the currents of particular QRPA states and thus highlight the main (e.g., collective) features of the nuclear flow in the given energy range. The procedure to get summed CTD is described in Ref. [57]. The summed CTD are shown in Fig. 8. The flow in left-right surface regions now more resembles the OSR picture. However, the flow is again mixed by isospin. It is isovector in the left-right sides and isoscalar in the pole regions.

Following WFM [28,29], the low-energy spin states should demonstrate out-of-phase rotation-like oscillations of spin-up and spin-down nuclear fractions; see Fig. 1(b). To check this prediction, we show in Figs. 9 and 10 spin-up and spin-down CTD for spin-flip states at 2.06 and 2.36 MeV. As seen from Table V, these states are almost fully exhausted by one proton and one neutron 2qp component, respectively. So, to characterize the nuclear flow in these states, the corresponding proton and neutron spin-up and spin-down currents are enough. Figures 9 and 10 show that the currents are not regular but rather demonstrate a complex cellular-like structure formed by the dominant 2qp configurations. They are proton $[411\uparrow, 411\downarrow]$ and neutron $[521\uparrow, 521\downarrow]$ configurations

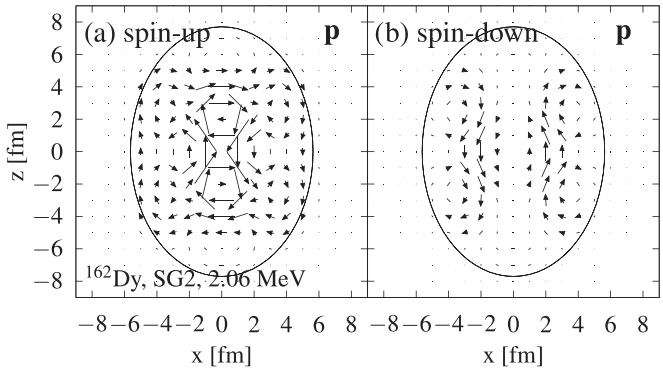

FIG. 9. Proton spin-up (a) and spin-down (b) CTD in basically proton 2.06-MeV state in ^{162}Dy.

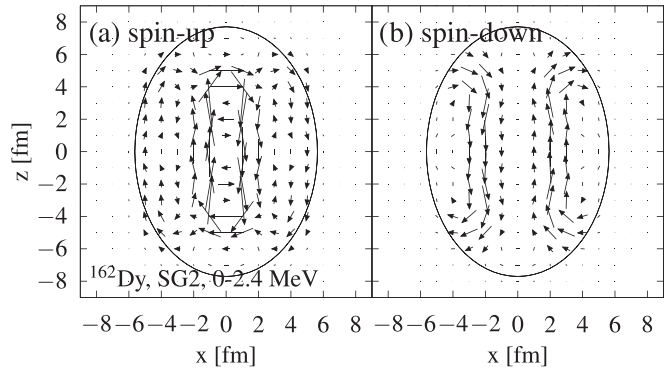

FIG. 11. Spin-up (a) and spin-down (b) CTD for the energy interval 0–2.4 MeV.

arising from $2d(l = 2)$ and $2f(l = 3)$ spherical subshells. Accordingly, the proton flow in Fig. 9 has a fewer number of cells than the neutron one in Fig. 10.

In Fig. 11, the summed CTD are depicted. They do not match regular collective WFM spin-scissors currents shown in Ref. [28].

C. $M1$ strength in ^{232}Th

In addition to strongly deformed Dy isotopes, SSR was also predicted by WFM in a less deformed nucleus ^{232}Th [25,26,28]. In this nucleus, the experiment [34] also gives two separate groups of low-energy 1^+ states [see Fig. 12(d)]. The lower group at $E < 2.5$ MeV is considered by WFM as a candidate for SSR. In this connection, we present QRPA results for ^{232}Th, obtained with the forces SVbas and SG2. Note that these forces, especially SG2, provide a good description of the spin-flip $M1$ giant resonance in ^{232}Th; see Appendix A.

In Fig. 12, the computed orbital, spin, and total $B(M1)$ strengths in ^{232}Th are compared with NRF experimental data [34]. We see that the spin strength is much smaller that the orbital one even at $E < 2.5$ MeV. For SG2, there is a remarkable agreement between the distribution of the total strength and the experimental data. Namely, both experiment and theory give at $E < 2.5$ MeV the distinctive group of the states. Figure 12 obviously *does not demonstrate any distinctive SSR*. Indeed, both level groups, below and above 2.5 MeV, are strongly dominated by the orbital strength. So, *these two groups are explained not by separation of SSR and OSR modes (as was suggested by WFM) but rather by a fine structure of the OSR alone.*

In Table VI, we show the features of some representative states with the large spin and orbital strength. In the SVbas case, the first state is not spin-flip one even though it has the largest spin strength at the range $E < 2.5$ MeV. Moreover, it is dominated by the orbital strength. This state is not collective and demonstrates a constructive interference of the spin and orbital contributions, in contrast to the lowest states in Dy isotopes. The 2.77-MeV state is collective and exhibits a constructive interference like the orbital states in Dy case. In the SG2 case, the first 1.96-MeV state is noncollective and mainly orbital (like for SVbas). The third 2.98-MeV state is spin-flip one with the dominant neutron configuration [631 ↑, 631 ↓]. Both states demonstrate a strong constructive interference of

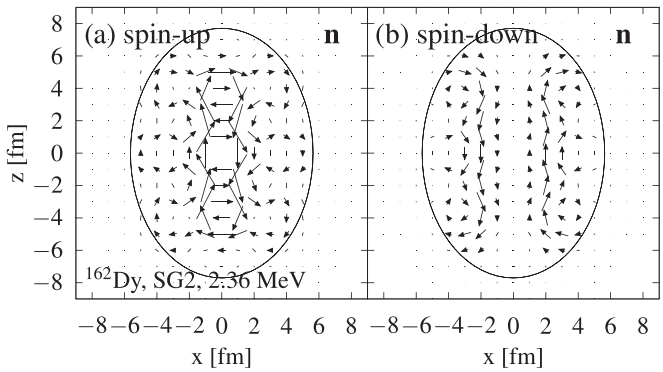

FIG. 10. The same as in Fig. 9 but for CTD in basically neutron 2.36-MeV state in ^{162}Dy.

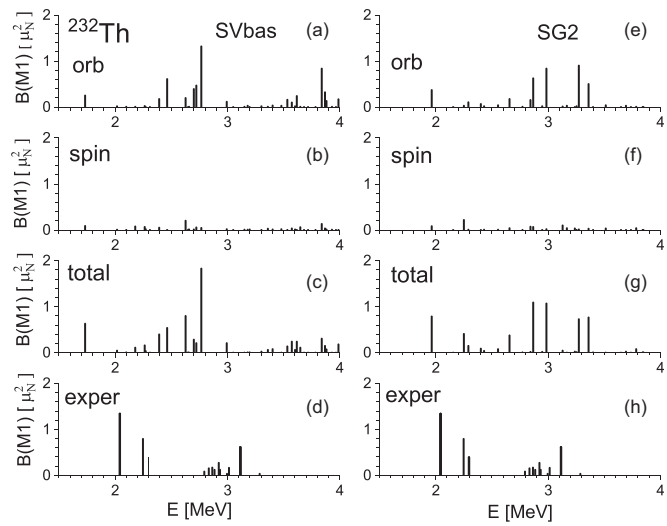

FIG. 12. The computed (SVbas, SG2) orbital, spin, and total low-energy $M1$ strengths in ^{232}Th as compared with the experimental data [34].

TABLE VI. The same as in Table V but for states in ^{232}Th.

Force	ν	E	$B(M1)$ $[\mu_N^2]$			Main 2qp components			
		[MeV]	Orb	Spin	Total	%	$[N, n_z, \Lambda]$	F position	Spher. limit
SVbas	1	1.73	0.25	0.09	0.63	91	pp [660 ↑, 651 ↑]	$F, F+1$	$1i_{13/2}, 1i_{13/2}$
	15	2.77	1.32	0.04	1.82	51	nn [761 ↑, 752 ↑]	$F-1, F-3$	$1j_{15/2}, 1j_{15/2}$
SG2	1	1.96	0.18	0.04	0.39	89	pp [660 ↑, 651 ↑]	$F, F+1$	$1i_{13/2}, 1i_{13/2}$
	3	2.25	0.01	0.11	0.20	96	nn [631 ↑, 631 ↓]	$F, F+3$	$1i_{13/2}, 3d_{5/2}$
	13	2.98	0.42	0.01	0.53	32	pp [530 ↑, 521 ↑]	$F-1, F+4$	$2f_{7/2}, 2f_{7/2}$

orbital and spin contributions. The 2.98-MeV state is a collective orbital state.

The calculated and experimental summed $M1$ strengths are compared in Table VII. Like in Dy isotopes, the theoretical values of the total $\sum B(M1)$ somewhat overestimate the experimental data. As mentioned in Sec. III A, the overestimation can be caused by (i) missing of a significant part of $M1$ strength in the experiment and (ii) neglect of the coupling with complex configurations. Like in Dy isotopes, we see in ^{232}Th the constructive interference of the spin and orbital contributions to the total strength.

IV. CONCLUSIONS

The WFM prediction of a low-energy spin-scissors resonance (SSR) in deformed nuclei [23,25–29] was analyzed in the framework of the self-consistent QRPA approach using Skyrme forces SkM*, SVbas, and SG2. The calculations were performed for deformed nuclei ^{160,162,164}Dy and ^{232}Th. Two of these nuclei, ^{164}Dy and ^{232}Th, were proposed by WFM as promising candidates for SSR.

The calculations have shown that in strongly deformed nuclei like ^{160,162,164}Dy, indeed there can exist a group of $K^\pi = 1^+$ spin states located at 1.5–2.4 MeV, i.e., below the conventional orbital scissor resonance (OSR). Following our analysis, these states are ordinary spin-flip excitations characterized by $M1(\Delta K = 1)$ transitions between spin-orbit partners in subshells with a low orbital momentum l, e.g., $2d$ and $1f$. Such low-l spin-flip states can form a separate low-energy group if a large deformation shifts OSR to a higher energy. In our calculations, this is the case for well deformed ^{160,162,164}Dy but not for less deformed ^{232}Th.

The obtained low-energy spin states are noncollective and mainly exhausted by one 2qp spin-flip configuration. This can be explained by the basically isovector character of the spin-spin residual interaction which upshifts the collectivity to higher energies. The noncollective character of low-energy spin states contradicts the collective scissors nature of the predicted SSR. Further, the calculated distributions of nuclear currents locally resemble the OSR collective flow but not the SSR one.

Since OSR energy $E \approx 66\delta A^{-1/3}$ MeV falls with the mass number A, this resonance in heavy (actinide) nuclei goes down by energy and mixes with nearby spin states. Being stronger, OSR conceals these states, so heavy deformed nuclei are not suitable to exhibit distinctive low-energy spin states.

At the excitation energy $E < 4$ MeV, most of 1^+ states demonstrate a significant interference of spin-flip and orbital contributions to $M1$ strength. The interference considerably increases the total $M1$ strength in the OSR energy range. This should be taken into account while comparing the computed strengths with estimations derived merely for the orbital mode. A part of the orbital strength is downshifted to the region of spin states ($E \leqslant 2.4$ MeV) and, vice versa, the OSR region hosts some spin-flip strength.

The experimental data [31–34] show two distinctive low-energy groups of 1^+ states in ^{162,164}Dy and ^{232}Th. These two groups are treated by WFM as SSR and OSR. Our calculations show that lowest 1^+ states in ^{160,162,164}Dy are indeed of spin-flip character. However, they are located at $E \leqslant 2.4$ MeV, i.e., below the observed states, so perhaps both observed groups are produced by fragmentation of the orbital strength. This is even more the case in ^{232}Th where the low-energy spin strength is almost negligible. So, in our opinion, *the available experimental data still do not confirm the existence of SSR*. More definite conclusions can be drawn after further experimental and theoretical effort. Indeed, following discussion [33], a significant number of 1^+ states can be found below 2.7 MeV; see database [49] for candidates. The theory should take into account the coupling with complex configurations, which, in principle, can redistribute the $M1$ strength.

The WFM *scissor-like* treatment of low-energy spin $M1$ excitations requires the nuclear deformation. In other words, spin-scissors excitations can exist only in deformed nuclei. Instead, our calculations show that low-energy spin states arise from the spin-orbit splitting and so can exist even in spherical nuclei. So *the deformation is not the origin of the low-energy spin strength* but only an essential factor affecting its properties. In principle, WFM does not use any two-rotor assumption. Then, perhaps, the deformation-induced scissors-like scheme is just a poorly chosen illustration.

The spin-orbit splitting and spin-spin residual interaction are of a primary importance in the exploration of spin

TABLE VII. The computed orbital, spin, and total $B(M1)$ strengths summed at $E = 0$–3.3 MeV as compared with the experimental data [34]. R are the interference factors.

Force	$\sum B(M1)[\mu_N^2]$				R
	Orb	Spin	Total	Exper.	
SVbas	3.60	0.66	5.23		1.23
SG2	3.37	0.68	4.92	4.26	1.21

excitations [4,5]. To check the accuracy of our QRPA method in describing these factors, we performed calculations for the spin-flip $M1(K = 1)$ giant resonance in ^{162}Dy and ^{232}Th and obtained for the forces SVbas and SG2 a good agreement with the experiment. The same test should be done by WFM as well.

In WFM calculations [27–29], the lowest $K^\pi = 1^+$ state with the energy $E = 1.47$ MeV has a huge quadrupole strength $B(E2) = 25.4$ W.u. The authors do not explain the origin of such state. By our opinion, this state is spurious. Neither experimental data nor our QRPA calculations for ^{160,162,164}Dy and ^{232}Th give at $E < 4$ MeV 1^+ states with so large $B(E2)$ value.

The discrepancy between WFM and QRPA predictions for spin states in ^{232}Th could be clarified by (p, p') measurements which are sensitive to spin-flip excitations and not so much to orbital ones. If low-energy spin states indeed exist in ^{232}Th, they should be observed in the (p, p') reaction.

Since low-energy spin states are reduced to almost pure 2qp excitations, these states can be useful for investigation of low-l spin-orbit splitting and its interplay with nuclear deformation. Besides, such states can be also useful for testing tensor forces.

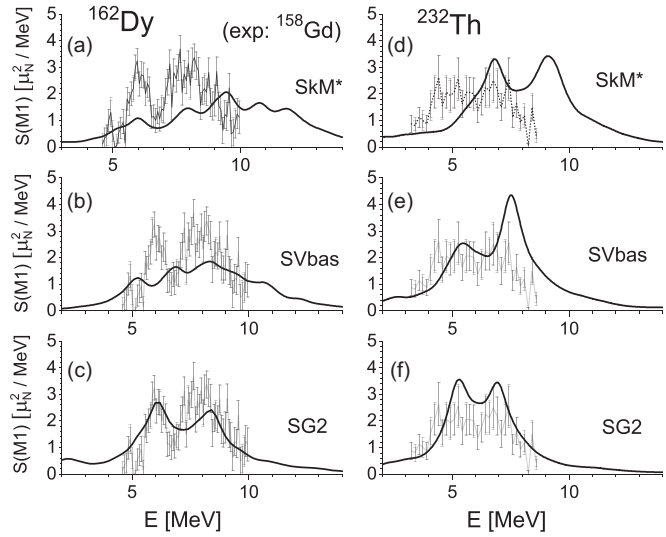

FIG. 13. $M1$ spin-flip giant resonance in ^{162}Dy and ^{232}Th, calculated with Skyrme forces SkM*, SVbas and SG2. The results are compared with scaled experimental data (in arbitrary units) for ^{232}Th [47,55] (right plots) and neighbouring nucleus ^{158}Gd [54] (left plots). See details in the text.

ACKNOWLEDGMENTS

We thank Prof. P.-G. Reinhard, Prof. P. von Neumann-Cosel, and Prof. A.V. Sushkov for useful discussions. The work was partly supported by a Votruba-Blokhintsev (Czech Republic–BLTP JINR) grant (V.O.N. and J.K.) and a grant of the Czech Science Agency, Project No. 19-14048S (J.K.), V.O.N. and W.K. appreciate the Heisenberg-Landau grant (Germany–BLTP JINR). A.R. acknowlegdes the support by the Slovak Research and Development Agency under Contract No. APVV-15-0225, Slovak grant agency VEGA (Contract No. 2/0067/21), and the Research and Development Operational Programme funded by the European Regional Development Fund (Project No. ITMS code 26210120023).

APPENDIX A: $M1$ SPIN-FLIP GIANT RESONANCE

Energy and structure of $M1$ spin-flip giant resonance in open-shell nuclei are basically determined by the interplay between spin-orbital splitting in proton and neutron schemes from one side and spin-spin residual interaction from another side [2,4,5]. To check the accuracy of our approach, we present here QRPA results for spin-flip giant resonance in ^{162}Dy and ^{232}Th, obtained with the Skyrme parametrizations SkM*, SVbas, and SG2. We were not able to find experimental data for this resonance in ^{162}Dy. So, for this nucleus, we compare QRPA results with the (p, p') data for the neighboring nucleus ^{158}Gd [54] which has a similar quadrupole deformations ($\beta_2 = 0.348$) [49]. For ^{232}Th, we use (p, p') data [47,55].

In Fig. 13, the results of our calculations are compared with the experimental data. QRPA strength functions are obtained by averaging transition rates $B_\nu(M1)$ for separate QRPA states by Lorentz weight with an averaging parameter $\Delta = 1$ MeV; see Refs. [4,5] for more detail. Only the spin part of $M1$ transition operator (3) is used. The experimental data (in arbitrary units) are properly scaled for a convenient comparison with QRPA strength functions. Figure 13 shows that SVbas and especially SG2 well describe localization and fine structure of the resonance in both nuclei. In SkM*, distribution of the strength is too wide and upshifted to higher energies. This difference can be explained by smaller values of spin-flip parameters b_4 and b'_4 in SVbas and SG2 sets (see Table I in Sec. II).

In Table VIII, the spin $B(M1)$ values summed at the energy interval $E = 0$–12 MeV are compared with early QRPA results of Sarriguren *et al.* [47], obtained with the force SG2. It is seen that the agreement is fine for SG2, acceptable for SVbas, and worse for SkM*.

Altogether, Fig. 13 and Table VIII show that forces SVbas and SG2 are most relevant for exploration of spin-flip excitations.

TABLE VIII. The strength $B(M1)_s$ summed at $E = 0$–12 MeV in our SkM*, SVbas, and SG2 calculations as compared with QRPA (SG2) results of Sarriguren *et al.* [47].

	$\sum B(M1)_s[\mu_N^2]$			
Nucleus	SkM*	SVbas	SG2	Sarriguren [47]
^{160}Dy	14.5	13.2	12.4	11.4
^{162}Dy	14.7	13.4	12.7	12.2
^{164}Dy	14.7	13.6	12.9	12.2
^{232}Th	17.2	15.9	14.3	14.9

APPENDIX B: WFM VS QRPA RESULTS

In this Appendix, we briefly discuss some important points concerning the comparison and treatment of WFM and QRPA results.

It is known that macroscopic and microscopic models often successfully supplement each other in description of nuclear modes [1,35]. For example, our QRPA results for isovector $E1$ giant resonance [56], $E1$ toroidal mode [57,58], and $M1$ orbital scissors (present calculations) well agree with predictions of macroscopic models (Refs. [59–61] and Refs. [10,15,16], respectively). However, we were not able to get a similar correspondence between our QRPA results and WFM predictions for SSR. In this connection, it is worth to discuss some important issues.

1. Accuracy of WFM numerical results for $M1$ low-energy spin states

Both Skyrme QRPA and WFM have spin-orbit mean-field terms and so include spin-orbit splitting and corresponding spin-flip excitations. In QRPA, spin-flip states are identified by strong domination of spin-flip 2qp components, large values of spin $B(M1)_s$, and hindered $B(E2)$. WFM deals with collective variables and identifies spin states mainly by enhanced $B(M1)$ and hindered $B(E2)$, where $B(M1)$ is calculated only for the total (spin+orbital) $M1$ operator. This seems not enough to identify reliably spin-flip states. Besides, following Table I for ^{164}Dy in Ref. [28], WFM does not produce at all the $M1$ spin-flip giant resonance, which makes questionable the accuracy of WFM in description of spin-flip states. Further, the parameters of the WFM Hamiltonian (includes a spherical harmonic oscillator, spin-orbit terms, pairing, quadrupole-quadrupole, and spin-spin separable residual interaction) are taken from different sources and, by our opinion, not properly justified. In this connection, the claimed good agreement of WFM results with the experimental data looks doubtful.

2. Is the spin-scissors scheme generally relevant?

The SSR macroscopic picture was suggested in analogy with OSR scheme developed within the two-rotor model [10,15,16]. However, the OSR scheme was confirmed by experimentally observed [13,14] specific dependencies of OSR energy and strength on the nuclear deformation [2,15,16]. Instead, the WFM calculations have not still suggested any specific measurable features justifying the relevance of the spin-scissors picture.

The spin-scissors picture assumes a nonzero nuclear deformation. Without deformation, this picture cannot be realized in principle. However, following our calculations, the deformation is not the primary origin of $M1$ low-energy spin states.

In the spin-scissors picture [Figs. 1(b) and 1(c)], SSR looks like a two-step process including spin-flip excitation + orbital oscillation. It is not clear how to match such a two-step process with the linear regime used in WFM. We have not found in Refs. [25–29] any relevant linear probe external field to generate such SSR.

Following Eq. (29) in Ref. [28], the WFM nuclear current is formed solely by components of an orbital collective variables for different combinations of spin directions. Maybe, for this reason, the currents for OSR, SSR-I, and SSR-II in Figs. 9–11 of Ref. [28] look identical (up to direction of the motion). Our QRPA distributions of the nuclear current partly support the isovector OSR scheme but not the SSR one.

Altogether, we have a feeling that the deformation-induced scissors-like picture used for illustration and interpretation of the WFM results is a poor and even misleading choice.

APPENDIX C: MATRIX ELEMENTS OF MAGNETIC TRANSITIONS IN AXIALLY DEFORMED NUCLEI

In cylindrical coordinates, the single-particle wave function with quantum numbers K^π has the spinor form

$$\Psi_i(\mathbf{r}) = \begin{pmatrix} R_i^{(+)}(\rho,z)e^{im_i^{(+)}\phi} \\ R_i^{(-)}(\rho,z)e^{im_i^{(-)}\phi} \end{pmatrix} \tag{C1}$$

for the normal state and

$$\Psi_{\bar{i}}(\mathbf{r}) = \hat{T}\Psi_i(\mathbf{r}) = \begin{pmatrix} -R_i^{(-)}(\rho,z)e^{-im_i^{(-)}\phi} \\ R_i^{(+)}(\rho,z)e^{-im_i^{(+)}\phi} \end{pmatrix} \tag{C2}$$

for the time-reversal state. Here the momentum projection is decomposed as $K_i = m_i^{(\sigma)} + \frac{1}{2}\sigma$ with $\sigma = \pm 1$.

The spin and orbital $M\lambda\mu$ transition operators are [62]

$$\hat{S}_{l\lambda\mu} = \mu_N\sqrt{\lambda(2\lambda+1)}r^l g_s^q\{\hat{\mathbf{s}}\,Y_l\}_{\lambda\mu}, \tag{C3}$$

$$\hat{L}_{l\lambda\mu} = \mu_N\sqrt{\lambda(2\lambda+1)}r^l g_l^q\frac{2}{\lambda+1}\{\hat{\mathbf{l}}\,Y_l\}_{\lambda\mu} \tag{C4}$$

where $l = \lambda - 1$, μ_N is the nuclear magneton, $\hat{\mathbf{s}}$ and $\hat{\mathbf{l}}$ are standard spin and orbital operators, and g_s^q and g_l^q are spin and orbital gyromagnetic factors. Further,

$$\{\hat{\mathbf{s}}\,Y_l\}_{\lambda\mu} = \sum_m\sum_{\alpha=-1,0,1} C^{\lambda\mu}_{lm,1\alpha}Y_{lm}\hat{s}_\alpha, \tag{C5}$$

$$\{\hat{\mathbf{l}}\,Y_l\}_{\lambda\mu} = \sum_m\sum_{\alpha=-1,0,1} C^{\lambda\mu}_{lm,1\alpha}Y_{lm}\hat{l}_\alpha, \tag{C6}$$

where Y_{lm} are the spherical harmonics and $C^{\lambda\mu}_{lm,1\alpha}$ are Clebsch-Gordan coefficients.

The matrix elements for the orbital and spin $M\lambda\mu$ transitions from the BCS vacuum $|\mathrm{BCS}\rangle$ to the two-quasiparticle (2qp) state $\alpha^+_i\alpha^+_{\bar{j}}|\mathrm{BCS}\rangle$ with the selection rule $|K_i - K_j| = \mu$ ($K_i, K_j > 0$, $\mu \geqslant 0$) have the form

$$\begin{aligned}\langle i\bar{j}|\hat{L}_{l\lambda\mu}|\mathrm{BCS}\rangle = 2\pi\mu_N\sqrt{\lambda(2\lambda+1)}\frac{2g_l}{\lambda+1}u^{(-)}_{ij}\int dzd\rho\rho\Bigg\{&g_{l\mu}\,C^{\lambda\mu}_{l\mu,10}\,[R^{(+)}_i m^{(+)}_j R^{(+)}_j + R^{(-)}_i m^{(-)}_j R^{(-)}_j]\\ &+\frac{1}{\sqrt{2}}g_{l\mu+1}\,C^{\lambda\mu}_{l\mu+1,1-1}\left[R^{(+)}_i\left(\rho\frac{d}{dz}-z\frac{d}{d\rho}-m^{(+)}_j\frac{z}{\rho}\right)R^{(+)}_j + R^{(-)}_i\left(\rho\frac{d}{dz}-z\frac{d}{d\rho}-m^{(-)}_j\frac{z}{\rho}\right)R^{(-)}_j\right]\\ &+\frac{1}{\sqrt{2}}g_{l\mu-1}\,C^{\lambda\mu}_{l\mu-1,11}\left[R^{(+)}_i\left(\rho\frac{d}{dz}-z\frac{d}{d\rho}+m^{(+)}_j\frac{z}{\rho}\right)R^{(+)}_j + R^{(-)}_i\left(\rho\frac{d}{dz}-z\frac{d}{d\rho}+m^{(-)}_j\frac{z}{\rho}\right)R^{(-)}_j\right]\Bigg\},\end{aligned} \tag{C7}$$

$$\begin{aligned}\langle i\bar{j}|\hat{S}_{l\lambda\mu}|\mathrm{BCS}\rangle = 2\pi\mu_N\sqrt{\lambda(2\lambda+1)}g_s u^{(-)}_{ij}\int dzd\rho\rho\,\Bigg\{&\frac{1}{2}g_{l\mu}\,C^{\lambda\mu}_{l\mu,10}\,[R^{(+)}_i R^{(+)}_j - R^{(-)}_i R^{(-)}_j]\\ &+\frac{1}{\sqrt{2}}g_{l\mu+1}\,C^{\lambda\mu}_{l\mu+1,1-1}R^{(-)}_i R^{(+)}_j - \frac{1}{\sqrt{2}}g_{l\mu-1}\,C^{\lambda\mu}_{l\mu-1,11}R^{(+)}_i R^{(-)}_j\Bigg\}.\end{aligned} \tag{C8}$$

Here $u^{(-)}_{ij} = u_i v_j - u_j v_i$ is the combination of Bogoliubov factors. The (ρ, z) dependence in the functions $R^{(\pm)}_i$, $g_{l\mu}$, and $g_{l\mu\pm1}$ is omitted for the sake of simplicity.

For the selection rule $K_i + K_j = \mu$, the matrix elements for the transitions to the 2qp state $\alpha^+_i\alpha^+_j|\mathrm{BCS}\rangle$ read

$$\begin{aligned}\langle ij|\hat{L}_{l\lambda\mu}|\mathrm{BCS}\rangle = 2\pi\mu_N\sqrt{\lambda(2\lambda+1)}\frac{2g_l}{\lambda+1}u^{(-)}_{ij}\int dzd\rho\rho\,\Bigg\{&g_{l\mu}\,C^{\lambda\mu}_{l\mu,10}\,[R^{(-)}_i m^{(+)}_j R^{(+)}_j - R^{(+)}_i m^{(-)}_j R^{(-)}_j]\\ &+\frac{1}{\sqrt{2}}g_{l\mu+1}\,C^{\lambda\mu}_{l\mu+1,1-1}\left[R^{(+)}_i\left(\rho\frac{d}{dz}-z\frac{d}{d\rho}+m^{(-)}_j\frac{z}{\rho}\right)R^{(-)}_j - R^{(-)}_i\left(\rho\frac{d}{dz}-z\frac{d}{d\rho}+m^{(+)}_j\frac{z}{\rho}\right)R^{(+)}_j\right]\\ &+\frac{1}{\sqrt{2}}g_{l\mu-1}\,C^{\lambda\mu}_{l\mu-1,11}\left[R^{(+)}_i\left(\rho\frac{d}{dz}-z\frac{d}{d\rho}-m^{(-)}_j\frac{z}{\rho}\right)R^{(-)}_j - R^{(-)}_i\left(\rho\frac{d}{dz}-z\frac{d}{d\rho}-m^{(+)}_j\frac{z}{\rho}\right)R^{(+)}_j\right]\Bigg\},\end{aligned} \tag{C9}$$

$$\begin{aligned}\langle ij|\hat{S}_{l\lambda\mu}|\mathrm{BCS}\rangle = 2\pi\mu_N\sqrt{\lambda(2\lambda+1)}g_s u^{(-)}_{ij}\int dzd\rho\rho\,\Bigg\{&\frac{1}{2}g_{l\mu}\,C^{\lambda\mu}_{l\mu,10}\,[R^{(+)}_i R^{(-)}_j + R^{(-)}_i R^{(+)}_j]\\ &+\frac{1}{\sqrt{2}}g_{l\mu+1}\,C^{\lambda\mu}_{l\mu+1,1-1}R^{(-)}_i R^{(-)}_j + \frac{1}{\sqrt{2}}g_{l\mu-1}\,C^{\lambda\mu}_{l\mu-1,11}R^{(+)}_i R^{(+)}_j\Bigg\}.\end{aligned} \tag{C10}$$

In (C7)–(C10), the functions g_{lm} ($m = \mu, \mu \pm 1$) are

$$g_{lm}(\rho, z) = r^l Y_{lm}(\theta, \phi)e^{-im\phi}. \tag{C11}$$

In our case of interest ($\lambda\mu = 11$), the transition operator has the form (3). In the above expressions, we have $l = 0$ and so only the terms with $\mu - 1 = 0$ survive. In these terms, $g_{l\mu-1}(\rho, z) \to g_{00} = 1/\sqrt{4\pi}$ and finally we get

$$\langle i\bar{j}|\hat{L}_{011}|\mathrm{BCS}\rangle = \sqrt{\frac{3\pi}{2}}\mu_N g_l u^{(-)}_{ij}\int dzd\rho\rho\left[R^{(+)}_i\left(\rho\frac{d}{dz}-z\frac{d}{d\rho}+m^{(+)}_j\frac{z}{\rho}\right)R^{(+)}_j + R^{(-)}_i\left(\rho\frac{d}{dz}-z\frac{d}{d\rho}+m^{(-)}_j\frac{z}{\rho}\right)R^{(-)}_j\right], \tag{C12}$$

$$\langle i\bar{j}|\hat{S}_{011}|\mathrm{BCS}\rangle = -\sqrt{\frac{3\pi}{2}}\mu_N g_s u^{(-)}_{ij}\int dzd\rho\rho R^{(+)}_i R^{(-)}_j, \tag{C13}$$

$$\langle ij|\hat{L}_{011}|\mathrm{BCS}\rangle = \sqrt{\frac{3\pi}{2}}\mu_N g_l u^{(-)}_{ij}\int dzd\rho\rho\left[R^{(+)}_i\left(\rho\frac{d}{dz}-z\frac{d}{d\rho}-m^{(-)}_j\frac{z}{\rho}\right)R^{(-)}_j - R^{(-)}_i\left(\rho\frac{d}{dz}-z\frac{d}{d\rho}-m^{(+)}_j\frac{z}{\rho}\right)R^{(+)}_j\right]\Bigg\}, \tag{C14}$$

$$\langle ij|\hat{S}_{011}|\mathrm{BCS}\rangle = \sqrt{\frac{3\pi}{2}}\mu_N g_s u^{(-)}_{ij}\int dzd\rho\rho R^{(+)}_i R^{(+)}_j. \tag{C15}$$

[1] M. N. Harakeh and A. van der Woude, *Giant Resonances* (Clarendon Press, Oxford, UK, 2001).

[2] K. Heyde, P. von Neumann-Cosel, and A. Richter, Rev. Mod. Phys. **82**, 2365 (2010).

[3] T. Lesinski, M. Bender, K. Bennaceur, T. Duguet, and J. Meyer, Phys. Rev. C **76**, 014312 (2007).

[4] P. Vesely, J. Kvasil, V. O. Nesterenko, W. Kleinig, P.-G. Reinhard, and V. Y. Ponomarev, Phys. Rev. C **80**, 031302(R) (2009).

[5] V. O. Nesterenko, J. Kvasil, P. Vesely, W. Kleinig, P.-G. Reinhard, and V. Y. Ponomarev, J. Phys. G: Nucl. Part. Phys. **37**, 064034 (2010).

[6] S. Goriely, S. Hilaire, S. Péru, M. Martini, I. Deloncle, and F. Lechaftois, Phys. Rev. C **94**, 044306 (2016).
[7] V. Tselyaev, N. Lyutorovich, J. Speth, P.-G. Reinhard, and D. Smirnov, Phys. Rev. C **99**, 064329 (2019).
[8] G. Kružić, T. Oishi, D. Vale, and N. Paar, Phys. Rev. C **102**, 044315 (2020).
[9] L.-G. Cao, G. Colò, H. Sagawa, P. F. Bortignon, and L. Sciacchitano, Phys. Rev. C **80**, 064304 (2009).
[10] N. Lo Iudice and F. Palumbo, Phys. Rev. Lett. **41**, 1532 (1978).
[11] R. R. Hilton, Z. Phys. A **316**, 121 (1984).
[12] D. Bohle, A. Richter, W. Steffen, A. E. L. Dieperink, N. Lo Iudice, F. Palumbo, and O. Scholten, Phys. Lett. B **137**, 27 (1984).
[13] W. Ziegler, C. Rangacharyulu, A. Richter, and C. Spieler, Phys. Rev. Lett. **65**, 2515 (1990).
[14] N. Lo Iudice and A. Richter, Phys. Lett. B **304**, 193 (1993).
[15] N. Lo Iudice, Phys. Part. Nucl. **28**, 556 (1997).
[16] N. Lo Iudice, Riv. Nuovo Cim. **23**, 1 (2000).
[17] A. E. L. Dieperink, Prog. Part. Nucl. Phys. **9**, 121 (1983).
[18] N. Lo Iudice and C. Stoyanov, Phys. Rev. C **65**, 064304 (2002).
[19] N. Pietralla, P. von Brentano, and A. F. Lisetskiy, Prog. Part. Nucl. Phys. **60**, 225 (2008).
[20] J. Enders, P. von Neumann-Cosel, C. Rangacharyulu, and A. Richter, Phys. Rev. C **71**, 014306 (2005).
[21] H. Pai, T. Beck, J. Beller, R. Beyer, M. Bhike, V. Derya, U. Gayer, J. Isaak, Krishichayan, J. Kvasil, B. Löher, V. O. Nesterenko, N. Pietralla, G. Martínez-Pinedo, L. Mertes, V. Y. Ponomarev, P.-G. Reinhard, A. Repko, P. C. Ries, C. Romig, D. Savran, R. Schwengner *et al.*, Phys. Rev. C **93**, 014318 (2016).
[22] M. Guttormsen, L. A. Bernstein, A. Bürger, A. Görgen, F. Gunsing, T. W. Hagen, A. C. Larsen, T. Renstrøm, S. Siem, M. Wiedeking, and J. N. Wilson, Phys. Rev. Lett. **109**, 162503 (2012).
[23] E. B. Balbutsev, I. V. Molodtsova, and P. Schuck, Nucl. Phys. A **872**, 42 (2011).
[24] E. B. Balbutsev, I. V. Molodtsova, and P. Schuck, Phys. Rev. C **91**, 064312 (2015).
[25] E. B. Balbutsev, I. V. Molodtsova, and P. Schuck, Phys. Rev. C **97**, 044316 (2018).
[26] I. V. Molodtsova and E. B. Balbutsev, Eur. Phys. J. Web Conf. **194**, 04004 (2018).
[27] E. B. Balbutsev, I. V. Molodtsova, and P. Schuck, Eur. Phys. J. Web Conf. **194**, 04005 (2018).
[28] E. B. Balbutsev, I. V. Molodtsova, A. V. Sushkov, N. Yu. Shirikova, and P. Schuck, arXiv:1902.05275.
[29] E. B. Balbutsev, I. V. Molodtsova, and P. Schuck, Phys. At. Nucl. **83**, 212 (2020).
[30] C. Wesselborg, P. von Brentano, K. O. Zell, R. D. Heil, H. H. Pitz, U. E. P. Berg, U. Kneissl, S. Lindenstruth, U. Seemann, and R. Stock, Phys. Lett. B **207**, 22 (1988).
[31] J. Margraf, T. Eckert, M. Rittner, I. Bauske, O. Beck, U. Kneissl, H. Maser, H. H. Pitz, A. Schiller, P. von Brentano, R. Fischer, R.-D. Herzberg, N. Pietralla, A. Zilges, and H. Friedrichs, Phys. Rev. C **52**, 2429 (1995).
[32] S. Valenta, B. Baramsai, T. A. Bredeweg, A. Couture, A. Chyzh, M. Jandel, J. Kroll, M. Krtička, G. E. Mitchell, J. M. O'Donnell, G. Rusev, J. L. Ullmann, and C. L. Walker, Phys. Rev. C **96**, 054315 (2017).
[33] T. Renstrøm, H. Utsunomiya, H. T. Nyhus, A. C. Larsen, M. Guttormsen, G. M. Tveten, D. M. Filipescu, I. Gheorghe, S. Goriely, S. Hilaire, Y.-W. Lui, J. E. Midtbø, S. Péru, T. Shima, S. Siem, and O. Tesileanu, Phys. Rev. C **98**, 054310 (2018).
[34] A. S. Adekola, C. T. Angell, S. L. Hammond, A. Hill, C. R. Howell, H. J. Karwowski, J. H. Kelley, and E. Kwan, Phys. Rev. C **83**, 034615 (2011).
[35] P. Ring and P. Schuck, *The Nuclear Many-Body Problem* (Springer-Verlag, New York, 1980).
[36] N. Van Giai and H. Sagawa, Phys. Lett. B **106**, 379 (1981).
[37] V. G. Soloviev, *Theory of Atomic Nuclei* (Pergamon Press, Oxford, UK, 1976).
[38] B. R. Mottelson and S. G. Nilsson, Mat. Fys. Skr. Dan. Vid. Selsk., Vol. 1, No. 8, 1959.
[39] M. Bender, P.-H. Heenen, and P.-G. Reinhard, Rev. Mod. Phys. **75**, 121 (2003).
[40] J. R. Stone and P.-G. Reinhard, Prog. Part. Nucl. Phys. **58**, 587 (2007).
[41] A. Repko, J. Kvasil, V. O. Nesterenko, and P.-G. Reinhard, arXiv:1510.01248.
[42] A. Repko, J. Kvasil, V. O. Nesterenko, and P.-G. Reinhard, Eur. Phys. J. A **53**, 221 (2017).
[43] A. Repko, J. Kvasil, and V. O. Nesterenko, Phys. Rev. C **99**, 044307 (2019).
[44] J. Kvasil, A. Repko, and V. O. Nesterenko, Eur. Phys. J. A **55**, 213 (2019).
[45] J. Bartel, P. Quentin, M. Brack, C. Guet, and H.-B. Håkansson, Nucl. Phys. A **386**, 79 (1982).
[46] P. Klüpfel, P.-G. Reinhard, T. J. Bürvenich, and J. A. Maruhn, Phys. Rev. C **79**, 034310 (2009).
[47] P. Sarriguren, E. Moya de Guerra, and R. Nojarov, Phys. Rev. C **54**, 690 (1996).
[48] P.-G. Reinhard, B. Schuetrumpf, and J. A. Maruhn, Comput. Phys. Commun. **258**, 107603 (2021).
[49] http://www.nndc.bnl.gov/nudat2/chartNuc.jsp.
[50] P.-G. Reinhard (private communication).
[51] M. Bender, K. Rutz, P.-G. Reinhard, and J. A. Maruhn, Eur. Phys. J. A **8**, 59 (2000).
[52] N. Pietralla, P. von Brentano, R.-D. Herzberg, U. Kneissl, J. Margraf, H. Maser, H. H. Pitz, and A. Zilges, Phys. Rev. C **52**, R2317 (1995).
[53] V. G. Soloviev, A. V. Sushkov, N. Y. Shirikova, and N. Lo Iudice, Nucl. Phys. A **600**, 155 (1996).
[54] D. Frekers, H. J. Wörtche, A. Richter, R. Abegg, R. E. Azuma, A. Celler, C. Chan, T. E. Drake, R. Helmer, K. P. Jackson, J. D. King, C. A. Miller, R. Schubank, M. C. Vetterli, and S. Yen, Phys. Lett. B **244**, 178 (1990).
[55] H. L. Wörtche, Ph.D. thesis, Technische Hochschule Darmstadt, Germany, 1994.
[56] W. Kleinig, V. O. Nesterenko, J. Kvasil, P.-G. Reinhard, and P. Vesely, Phys. Rev. C **78**, 044313 (2008).
[57] A. Repko, P.-G. Reinhard, V. O. Nesterenko, and J. Kvasil, Phys. Rev. C **87**, 024305 (2013).
[58] A. Repko, V. O. Nesterenko, J. Kvasil, and P.-G. Reinhard, Eur. Phys. J. A **55**, 242 (2019).
[59] M. Goldhaber and E. Teller, Phys. Rev. **74**, 1046 (1948).
[60] H. Steinwedel and J. H. D. Jensen, Z. Naturforsch. **5**, 413 (1950).
[61] S. F. Semenko, Sov. J. Nucl. Phys. **34**, 356 (1981).
[62] A. Bohr and B. R. Mottelson, *Nuclear Structure*, Vol. 1 (Benjamin, New York, 1969).

Correction: An inline equation appearing in the first paragraph of Appendix C contained an error and has been fixed.